Supporting Information for "Coexistence of two dune growth mechanisms in a landscape-scale experiment"

Ping Lü[1], Clément Narteau[2,*], Zhibao Dong[1], Philippe Claudin[3], Sébastien Rodriguez[2], Zhishan An[4], Cyril Gadal[2], Sylvain Courrech du Pont[5]

[1] School of Geography and Tourism, Shaanxi Normal University, 620 Chang'an West Avenue, Xi'an, Shaanxi 710119, China.

[2] Université de Paris, Institut de physique du globe de Paris, CNRS, F-75005 Paris, France.

[3] Physique et Mécanique des Milieux Hétérogènes, UMR 7636 CNRS, ESPCI PSL Research Univ, Sorbonne Univ, Université de Paris, 10 rue Vauquelin, 75005 Paris, France.

[4] Northwest Institute of Eco-Environment and Resources Donggang West Road 320, Lanzhou, Gansu Province 730000, China.

[5] Laboratoire Matière et Système Complexes, Université de Paris. UMR 7057 CNRS, Bâtiment Condorcet, 10 rue Alice Domon et Léonie Duquet, 75205 Paris Cedex 13, France.

*Corresponding authors: narteau@ipgp.fr and lvping@lzb.ac.cn

Contents

List of Figures

List of Tables

1 Supporting Text 1
Grain size distribution

The landscape-scale experiment site is located close to the oasis city of Shapotu at 8 km from the Yellow River in the Tengger desert, which covers an area of about 36,700 km^2 in the northwest part of the Zhongwei County in the Ningxia Hui Autonomous Region of the People's Republic of China (37°31'N, 105°E). This desert is characterised by a lognormal grain size distribution with a mean value d=190 μm (Fig. S1).

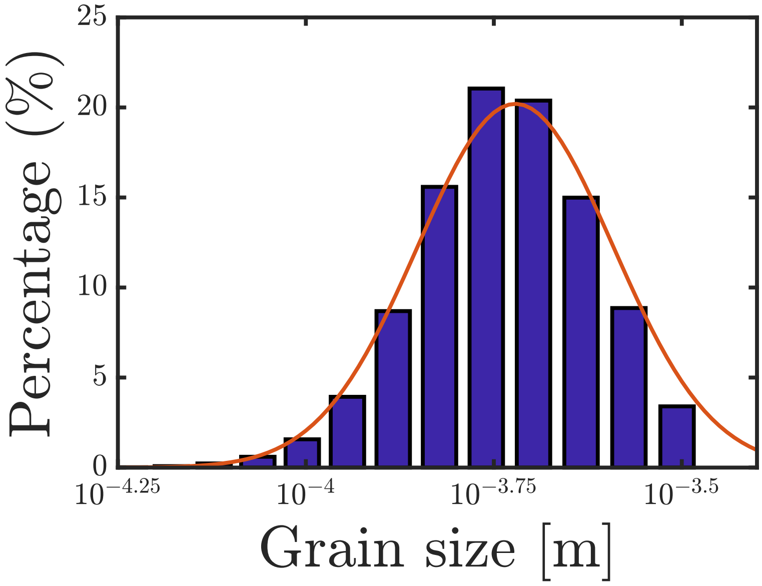

Figure S1: Grain size distribution in the Tengger desert. The line is the best fit using a lognormal distribution with a mean value $d = 190\ \mu\text{m} \approx 10^{-3.72}$ m.

2 Supporting Text 2
Wind data and characterization of the local wind regime

We installed a 2 m high wind tower in the center of the experimental site and collected the wind data of the local airport located 10 km east.

Comparison of wind data

Fig. S2a shows the distribution of the divergence angle between the wind orientation measured locally and by the airport meteorological tower. There is systematic shift of 14° between these two data sets, which can be explained by differences between the alignments of the wind vanes and the accuracy of the measurement of the airport meteorological tower (±10°).

Fig. S2b shows the shear velocity derived from a local wind measurement, the 2 m high wind tower and the airport meteorological tower during the transport threshold experiment (see Fig. 2 of Lü et al., 2021). All these data are consistent with each other. As a consequence, the threshold shear stress derived from the local measurement can be extrapolated to other wind data to compute sand fluxes and the subsequent dune properties (Sec. 3.1).

In order to compare to observations over the four years of the landscape-scale experiment,

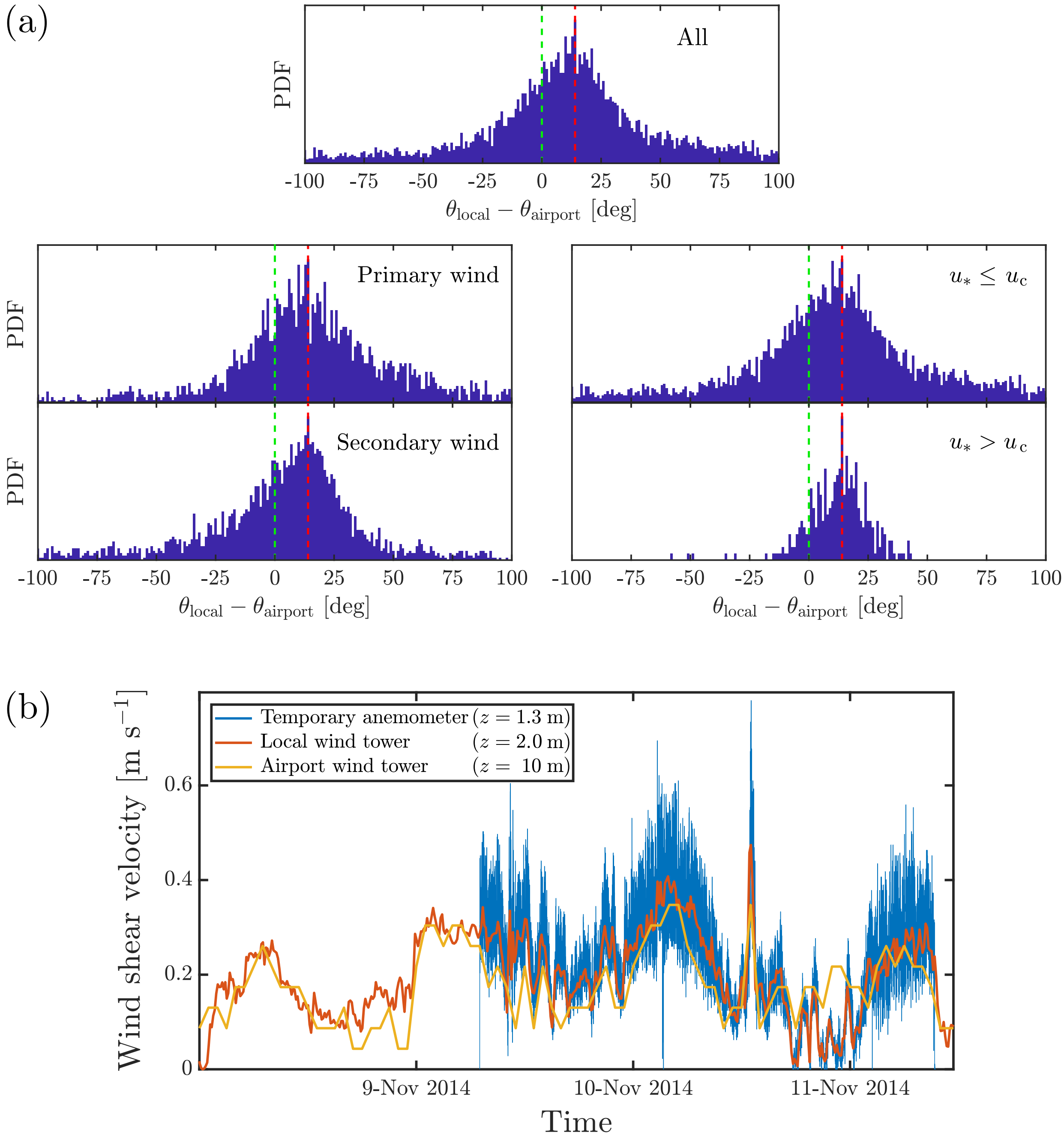

Figure S2: Comparison of wind data. **(a)** Distribution of the divergence angle between the wind orientation measured in the experimental site by a 2 m high wind tower and the airport meteorological tower. There is systematic shift of 14^{o} (dashed lines). **(b)** Wind shear velocity derived from temporary wind speed measurements during the threshold experiment (blue, see Lü et al., 2021, for more details) and simultaneous measurements on the local (red) and the airport wind towers (green). There is a general agreement between all these data sets.

we only use the wind data of the local airport rotated 14^o clockwise because the record is more continuous and spans a longer period.

Characterization of the wind regime.

Raw wind data shows lot of variability in direction and strength reflecting the turbulent character of the air flow in this area. Nevertheless, there is a dominant bimodal wind regime resulting from the global climatic forcing in the Tengger desert.

We use an Expectation-Maximization (EM) algorithm (Dempster et al., 1977) to fit the flux orientation distribution by a Gaussian mixture model. Thus, we replace the real flux data by a limited number n_Θ of normal distributions characterized by mean orientations Θ_i, standard variations s_i and weights w_i with $i = \{1, \ldots, n_\Theta\}$. Considering only time periods during which the wind velocity is above a critical value for sediment transport (i.e. $u_* > u_c$, see Eq. 4), we assume that the probability density function of sand flux orientation Θ may be described by a sum of normal distributions :

$$\mathcal{P}(\Theta) = \sum_{i=1}^{n_\Theta} \frac{w_i}{s_i\sqrt{2\pi}} \exp\left(-\frac{(\Theta-\Theta_i)^2}{2s_i^2}\right). \tag{1}$$

The Expectation-Maximization (EM) algorithm is a natural generalization of maximum likelihood estimation to the incomplete data case. This is an iterative scheme that includes two different steps. Starting from initial guesses for the parameters w_i, s_i and Θ_i, the (first) Expectation-step is to compute a probability distribution over possible completions. In the (second) Maximization-step, new parameters are determined using the current completions. These steps are repeated until convergence.

Using the wind data from the airport from January 1, 2013 to December 31, 2017, Fig. S3 shows how the sand flux orientation can be fitted with a two component Gaussian mixture model ($n_\Theta = 2$). Mean orientations, standard deviations and weights for the wind tower of the airport are

$$\Theta_1 = 323.6^o, \qquad w_1 = 0.6, \qquad s_1 = 24.9^o.$$

$$\Theta_2 = 177.7^o, \qquad w_2 = 0.4, \qquad s_2 = 18.6^o.$$

All angles are measured anticlockwise from east. The primary wind comes from the northwest, the secondary wind from the east. We can estimate the transport ratio $N = w_1/w_2 = 1.5$ as well as the angle of divergence $\Theta = 145.9^o$ between the primary and secondary winds. All these values agree with those computed from the wind data of the local meteorological tower from January 1, 2008 to December 31, 2011 (see Ping et al., 2014).

3 Supporting Text 3
Sand flux and dune orientations

Wind data are used to predict sand flux properties on a flat sand bed and a set of variables relevant for dune morphodynamics: orientation, sand flux at the crest, migration direction and dune-height growth rate. Tab. S1 shows the results obtained using the formalism that follows.

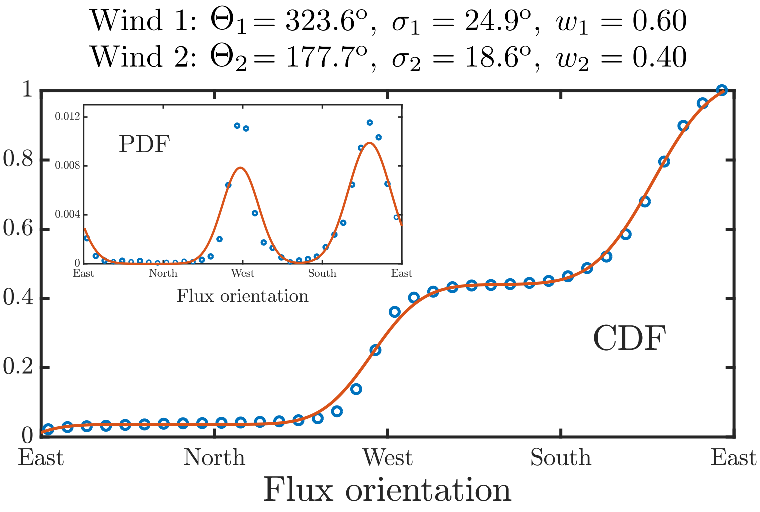

Figure S3: Distribution of sand flux orientation. The cumulative density function (CDF) of sand flux orientation (blue circles) and the best fit using a two-component Gaussian mixture model (red line). The inset shows the probability density function (PDF).

3.1 Saturated flux on a flat sand bed

Wind measurements provide the wind speed u_i and direction $\vec{x}_i$ at different times t_i, $i \in [1; N]$. For each time step i, the shear velocity writes

$$u_*^i = \frac{u_i \kappa}{\log(z/z_s)}, \tag{2}$$

where z is the height at which the wind velocity u_i has been measured and κ the von-Kármán constant. Instead of the geometric roughness that depends only on grain size, we consider here the aerodynamic roughness $z_\mathrm{s} = 10^{-3}$ m that accounts for the height of the transport layer in which saltating grains modify the vertical wind velocity profile. The same value for the aerodynamic roughness can also be determined from the Owen (1964) formula, $C\langle u_* \rangle^2/(2g)$, where the constant C is taken equal to 0.25 to account for its higher value on dunes with superimposed ripples during periods with saltation (Sherman & Farrell, 2008; Field & Pelletier, 2018). The value of the threshold shear velocity for motion inception is determined using the formula calibrated by Iversen and Rasmussen (1999)

$$u_\mathrm{c} = 0.1\sqrt{\frac{\rho_\mathrm{s}}{\rho_\mathrm{f}} gd}. \tag{3}$$

Using the gravitational acceleration g, the grain to fluid density ratio $\rho_\mathrm{s}/\rho_\mathrm{f} \simeq 2.05 \times 10^3$ and the grain diameter $d = 190\,\mu$m, we find $\mathrm{u_{th}} = 0.19\,\mathrm{m\,s^{-1}}$, which corresponds to a threshold wind speed $u_{10} = 4.4\,\mathrm{m\,s^{-1}}$ ten meters above the ground. It is close to the values measured in the field, which are $u_\mathrm{th} = 0.23 \pm 0.04$ and $u_{10} = 5.3 \pm 0.92\,\mathrm{m\,s^{-1}}$ (see Fig. 2 in Lü et al., 2021).

For each time step i, the saturated sand flux $\overrightarrow{Q_i}$ on a flat sand bed is computed from the relationship proposed by Ungar and Haff (1987) and calibrated by Durán et al. (2011):

$$Q_\mathrm{sat}(u_*) = \begin{cases} 25\,\dfrac{\rho_\mathrm{f}}{\rho_\mathrm{s}}\sqrt{\dfrac{d}{g}}\left(u_*^2 - u_\mathrm{c}^2\right) & \text{for } u_* > u_\mathrm{c}, \\ 0 & \text{else.} \end{cases} \tag{4}$$

In this formula, the prefactor takes into account a dune compactness of 0.6.

From the individual saturated sand flux vectors $\overrightarrow{Q_i}$, we estimate the mean sand flux vector on

Variable	Units	Value
Acceleration of gravity g	$\mathrm{m\,s^{-2}}$	9.81
Grain size d	m	190×10^{-6}
Air density ρ_f	$\mathrm{kg\,m^{-3}}$	1.29
Grain density ρ_s	$\mathrm{kg\,m^{-3}}$	2.55×10^{3}
Aerodynamic roughness z_s	m	10^{-3}
von-Kármán constant κ	$\emptyset$	0.4
Shear velocity and sand flux on a flat sand bed		
Threshold shear velocity u_c	$\mathrm{m\ s^{-1}}$	0.19
Mean shear velocity $\langle u_* \rangle$	$\mathrm{m\ s^{-1}}$	0.29
$\langle u_* \rangle / u_\mathrm{c}$	$\emptyset$	1.5
$\mathrm{DP} = \langle \Vert \overrightarrow{Q} \Vert \rangle$	$\mathrm{m^2\ yr^{-1}}$	18.4
$\mathrm{RDP} = \Vert \langle \overrightarrow{Q} \rangle \Vert$	$\mathrm{m^2\ yr^{-1}}$	5.7
RDP/DP	$\emptyset$	0.32
RDD	mod 360°	280.6
Dune orientation and sand flux at the crest		
Dune orientation α_I	mod 180°	68.3
Dune orientation α_F	mod 360°	272.8
$\Delta\alpha = \alpha_\mathrm{I} - \alpha_\mathrm{F}$	°	-24.5
$\Vert \langle \overrightarrow{Q_\mathrm{I}} \rangle \Vert$	$\mathrm{m^2\ yr^{-1}}$	13.4
$\Vert \langle \overrightarrow{Q_\mathrm{F}} \rangle \Vert$	$\mathrm{m^2\ yr^{-1}}$	11.1
$\Vert \langle \overrightarrow{Q_\mathrm{F}} \rangle \Vert / \Vert \langle \overrightarrow{Q_\mathrm{I}} \rangle \Vert$	$\mathrm{m^2\ yr^{-1}}$	0.83
Direction of $\langle \overrightarrow{Q_\mathrm{I}} \rangle$	mod 360°	282.7
Direction of $\langle \overrightarrow{Q_\mathrm{F}} \rangle$	mod 360°	α_F
$\Delta\alpha_\mathrm{Q}$	°	-9.9
$\sigma_\mathrm{F}/\sigma_\mathrm{I}$	$\emptyset$	0.88

Table S1: Shear velocity, sand fluxes and dune orientations derived from the airport wind data from January 1, 2013 to October 31, 2017. See text and Eqs. 2-16 for the description of all variables. All angles are measured counterclockwise from East. Following Gao et al. (2015), the wind speed-up have been computed with $\gamma = 1.6$. Dune orientations show variation of 10° with respect to the γ-value, from $\gamma = 0$ to $\gamma \to \infty$. $\Delta\alpha_\mathrm{Q}$ is the angle between $\langle \overrightarrow{Q_\mathrm{I}} \rangle$ and $\langle \overrightarrow{Q_\mathrm{F}} \rangle$. By definition, $\{\Delta\alpha, \Delta\alpha_\mathrm{Q}\} \in [-90^\circ, 90^\circ]$. These variables predict the formation of oblique dunes in the bed instability mode (Ping et al., 2014),

$\alpha_\mathrm{I} - \mathrm{RDD} = 32.3^\circ \pmod{90^\circ}$,

and the formation of longitudinal dunes in the elongating mode, also defined as the fingering mode by Courrech du Pont et al. (2014),

$\alpha_\mathrm{F} - \mathrm{RDD} = 7.8^\circ \pmod{180^\circ}$

(see Fig. 4 of the main manuscript).

a flat erodible bed

$$\langle \overrightarrow{Q} \rangle = \frac{1}{N} \sum_{i=1}^{N} \overrightarrow{Q_i}. \tag{5}$$

The norm of the mean sand flux is usually called the resultant drift potential:

$$\mathrm{RDP} = \Vert \langle \overrightarrow{Q} \rangle \Vert. \tag{6}$$

This quantity is highly dependent on the wind regime. Since it is a vectorial sum, the contributions of winds from opposite directions cancel each other out. Hence, for the entire time period, we also calculate the drift potential,

$$\mathrm{DP} = \frac{1}{N} \sum_{i=1}^{N} \left\Vert \overrightarrow{Q_i} \right\Vert \tag{7}$$

This mean sand flux does not take into account the orientation of the individual sand fluxes computed from the successive wind measurements (Fryberger & Dean, 1979).

The ratio RDP/DP is a non-dimensional parameter, which is often used to characterize the directional variability of the wind regimes (Pearce & Walker, 2005; Tsoar, 2005): RDP/DP $\rightarrow 1$ indicates that sediment transport tends to be unidirectional; RDP/DP $\rightarrow 0$ indicates that most of the transport components cancel each other out. Finally, RDD is the resultant drift direction, i.e., the direction of $\langle \overrightarrow{Q} \rangle$.

The mean shear velocity $\langle u_* \rangle$ is defined as the shear velocity averaged over the transport periods. i.e. when $Q_{\text{sat}} > 0$. Using the Heaviside function H_u defined as

$$H_u = \begin{cases} 1 & \text{for } u_* > u_{\text{c}}, \\ 0 & \text{else}, \end{cases} \tag{8}$$

the mean shear velocity can be directly computed from the shear velocity

$$\langle u_* \rangle = \sum_{i=1}^{N} H_u^i u_*^i \Big/ \sum_{i=1}^{N} H_u^i, \tag{9}$$

or from the integrated flux using the inverse function Q_{sat}^{-1} of the transport law (Eq. 4):

$$\langle u_* \rangle = Q_{\text{sat}}^{-1} \left(\text{DP} \Big/ \sum_{i=1}^{N} H_u^i \right). \tag{10}$$

We calculated the values of $\langle u_* \rangle$ both ways and we did not find significant differences considering wind data from the Tengger desert.

3.2 The transport deficit

All variables described above are usually used with the wind and sand flux roses to estimate transport properties over a given period of time. Nevertheless, these integrated quantities provide little information on the different phases of transport and the wind sequence. In order to describe these various stages and identify the annual transport cycle in terrestrial deserts, we analyze the fluctuations of the cumulative transport vector $\sum \overrightarrow{Q_i}$ with respect to the average trend estimated from the mean sand flux vector $\sum \langle \overrightarrow{Q} \rangle$ (Fig. S4a). In practice, the transport deficit is defined as

$$\mathcal{S}_n = n \| \langle \overrightarrow{Q} \rangle \| - \sum_{i=1}^{n} \overrightarrow{Q_i} \cdot \overrightarrow{e}_{\langle \overrightarrow{Q} \rangle}, \tag{11}$$

where $\overrightarrow{e}_{\langle \overrightarrow{Q} \rangle}$ is the dimensionless unit vector of the mean sand flux vector, which has the same direction as the RDD. Note that $1 \leq n \leq N$ is the index of the successive wind measurements and corresponds to time. Thanks to the scalar product, the $\mathcal{S}$-value measures the difference between the current and the mean cumulative transport, both in terms of orientation and intensity. This is the integral of the fluctuations around the mean transport vector.

To help in interpreting the temporal fluctuation of $\mathcal{S}$ in natural environments, some basic properties are summarized below using schematic wind regimes shown in Fig. S4b-e:

- By definition, $\mathcal{S} = 0$ at the beginning and the end of studied period.

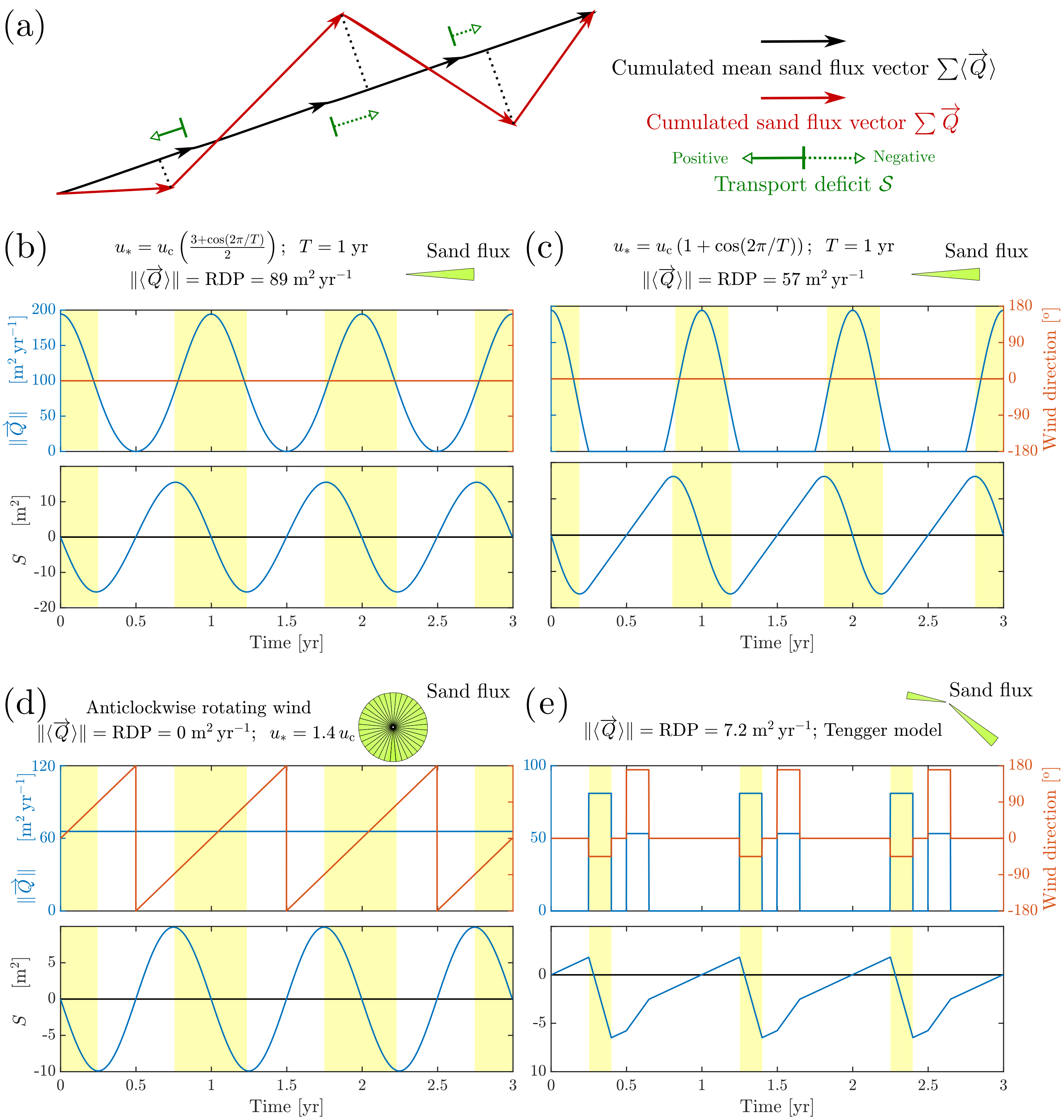

Figure S4: The transport deficit $\mathcal{S}$ with respect to time under schematic wind regimes. (a) Example illustrating for 4 time steps the transport deficit calculation method. **(b)** Unidirectional wind regime with sinusoidal wind speed above the transport threshold. **(c)** Unidirectional wind regime with sinusoidal wind speed above and below the transport threshold. **(d)** Constant wind speed in a rotating wind regime. **(e)** Bidirectional wind regime representative of the Tengger desert. Top figures in **(a-d)** show the norm and orientation of the sand flux vector with respect to time. See also the sand flux roses (insets). All angles are measured counterclockwise from East. In all cases, the highlighted time periods correspond to a decreasing transport deficit, i.e. periods during which the current transport vector contributes positively to the average transport vector. For **(c)**, $\vec{e}_{\langle\vec{Q}\rangle}$ is arbitrarily oriented to the East.

- If there is a wind cycle, typically one year in terrestrial desert, the duration over which the mean transport properties are estimated should be an integer multiple of the observed wind period. In this case, the range of computed $\mathcal{S}$-value depends on the time at which the data began to be collected. The range of computed $\mathcal{S}$-values extends more to negative than positive values if data collection began after a period of weaker winds, and vice versa.
- Under unidirectional wind regime (Fig. S4b-c), there is a perfect negative linear correlation between the variation of the transport deficit and the transport rate, i.e., $\partial\mathcal{S}/\partial t = RDP - \|\overrightarrow{Q}\|$.
- Under multidirectional wind regimes (Fig. S4d), the transport deficit increases faster than RDP when there is a negative projection of the current flux vector on the resultant sand flux vector (i.e., $\overrightarrow{Q} \cdot \overrightarrow{e}_{\langle\overrightarrow{Q}\rangle} < 0$ in Eq. 11).
- The transport deficit $\mathcal{S}$ can be used to characterize planetary wind regimes because it takes into account both the orientation and the magnitude of the sand flux over a given time period. Using a simplified version of the wind regime observed in the Tengger desert, Fig. S4e shows how the two dominant winds can be recognized in variations of the transport deficit. This figure has to be compared to Fig. 1d of the main manuscript.

3.3 The increase in sand flux at the crest of dunes

A positive topography accelerates wind speed, so that the sand flux over a dune depends on the dune shape. For 2D turbulent flows over low hills, Jackson and Hunt (1975) show that the increase of wind velocity at the top of the hill, the so-called speed-up factor, is approximately proportional to the hump aspect ratio. Hence, at the first order of the dune aspect ratio, the sand flux $\overrightarrow{Q_i^c}$ at the crest of the dune writes

$$\overrightarrow{Q_i^c} = \overrightarrow{Q_i}\left(1 + \gamma\left|\sin\left(\theta_i - \alpha\right)\right|\right), \tag{12}$$

where α is the orientation of the linear dune, $\overrightarrow{Q_i}$ the saturated sand flux vector on a flat sand bed, θ_i the orientation of this flux vector and γ the flux-up ratio:

$$\gamma = \beta\frac{H}{W}. \tag{13}$$

W is the width of the dune, H its height and β a dimensionless coefficient that accounts for all the other physical ingredients (e.g., roughness) that affect the speed-up.

3.4 Dune orientation and sand flux at dune crests

Dune orientation α_{I} in the bed instability mode

In the bed instability mode, dunes grow in height from the erosion of the sand bed in the interdune areas. Thus, linear bedforms develop perpendicularly to the direction for which the normal-to-crest component of transport is maximum (Rubin & Hunter, 1987).

Considering the orientation θ_i of fluxes $\overrightarrow{Q_i^c}$, we calculate $Q_\perp(\alpha)$, the total sand flux perpendicular to the crest for all possible crest orientations $\alpha \in [0; \pi]$. Then, we identify the maximum value of

$Q_\perp(\alpha)$ that corresponds to the most probable crest orientation α_I of dunes in the bed instability mode. Note that this procedure is the same as the gross bedform-normal transport rule of Rubin and Hunter (1987), except that we take into account the increase of the sand fluxes at the crest of dunes (i.e., $\gamma \neq 0$). As detailed in Courrech du Pont et al. (2014) and Gao et al. (2015), it may significantly change the predictions of dune orientation.

Dune orientation α_F in the elongating mode

In the elongating mode, dunes extend in the direction of the resultant sand flux at the crest. Hence, the orientation α_F selected by the elongation mechanism is the one for which the normal-to-crest components of transport cancel each other out.

In practice, we calculate $Q_\perp(\alpha)$ and $Q_\parallel(\alpha)$, the total sand flux perpendicular and parallel to the crest for all possible crest orientations $\alpha \in [0; 2\pi]$. Then, we select the orientation α_F for which the sediment flux perpendicular to the crest vanishes (i.e., $Q_\perp(\alpha) = 0$) and for which the flux parallel to the dune is positive (i.e., $Q_\parallel(\alpha) > 0$). If more than one solution exists, we look for the angle at which the $Q_\parallel$-value is maximum. By definition, when there is no feedback of topography on the flow (i.e., $\gamma = 0$ in Eq. 12), the orientation of the linear dune in the elongating mode α_F is given by the resultant sand transport direction (also called the RDD). When the wind speed-up is taken into account, the dune orientation depends on the γ-value. As shown in numerical simulations by Gao et al. (2015), $\gamma = 1.6$ gives reasonable estimates of dune orientation.

Classification of dune orientation

Following Hunter et al. (1983), the classification of dune orientation is based on the angle between crest alignment and the resultant sand flux on a flat sand bed. Dunes are transverse when this angle is larger than 75°, longitudinal when it is smaller than 15° and oblique in all the other cases. Dunes in the bed instability mode can be transverse, oblique or longitudinal. Elongating dunes can only be longitudinal or oblique (Courrech du Pont et al., 2014). From the predicted crest orientations α_I and α_F in the bed instability and the elongating modes, respectively, we calculate

$$\Delta\alpha = \alpha_\mathrm{I} - \alpha_\mathrm{F}, \tag{14}$$

the angle between the two bedform alignments ($\Delta\alpha \in [-\pi/2; \pi/2]$).

Sand flux at the crest of dunes in the bed instability and elongating modes

Because the apparent dune aspect-ratio (i.e., the aspect ratio seen by the wind) determines the increase in wind speed at the top of the dune, the magnitude and the orientation of the mean sand flux at the dune crest $\overrightarrow{Q_{\{\mathrm{I,F}\}}}$ is a function of dune orientation $\alpha_{\{\mathrm{I,F}\}}$:

$$\overrightarrow{Q_{\{\mathrm{I,F}\}}} = \frac{1}{N}\sum_{i=1}^{N} \overrightarrow{Q_i}\left(1 + \gamma\left|\sin\left(\theta_i - \alpha_{\{\mathrm{I,F}\}}\right)\right|\right), \tag{15}$$

where θ_i is the orientation of the flux $\overrightarrow{Q_i}$ on a flat sand bed. Then, $\Delta\alpha_\mathrm{Q}$ is the angle between the direction of the resultant sand flux at the crest of dunes in the bed instability and the elongating modes ($\Delta\alpha_{\mathrm{Q}} \in [0;\pi]$). The angles $\Delta\alpha$ and $\Delta\alpha_{\mathrm{Q}}$ are critical in dune morphodynamics when considering the development of superimposed bedforms in the bed instability mode on the flanks of dunes in the elongating mode (Lü et al., 2017).

Dune-height growth rate

All sand fluxes perpendicular to the crest can contribute to dune growth. Considering the dune orientation $\alpha_{\{\mathrm{I,F}\}}$, we calculate the relative growth rate $\sigma_{\{\mathrm{I,F}\}}$ to build up a linear dune of height H and width W in the bed instability or the elongating mode (Gao et al., 2015; Courrech du Pont et al., 2014):

$$\sigma_{\{\mathrm{I,F}\}} = \frac{1}{NHW}\sum_{i=1}^{N}\left\|\overrightarrow{Q_i}\right\|\left(1+\gamma\left|\sin\left(\theta_i-\alpha_{\{\mathrm{I,F}\}}\right)\right|\right)\left|\sin\left(\theta_i-\alpha_{\{\mathrm{I,F}\}}\right)\right|. \tag{16}$$

This expression is normalized by dune size and relies only on a macroscopic description of both the dune geometry and the flow (Courrech du Pont et al., 2014). Nevertheless, considering incipient dunes in the bed instability mode and the most unstable wavelength for the formation of dunes, this growth rate can be related to the growth rate $\sigma(\lambda_{\max})$ of the most unstable mode of the dune instability (Lü et al., 2021). A full description of the dune instability in multidirectional wind regime can be found in Gadal et al. (2019).

4 Supporting Text 4
Two modes of dune orientation

The landscape-scale experiments presented have been designed to observe simultaneous development of dunes in the two dune growth mechanisms, defined as bed instability and the elongating modes by Courrech du Pont et al. (2014). With an angle of divergence of about 150°, a transport ratio of 3/2, a growth rate ratio $\sigma_{\mathrm{F}}/\sigma_I = 0.88$ and frequent wind reversals (see Tab. S1 and Sec. 2), the wind regime in the Tengger desert meets all the conditions required for the coexistence of the two dune growth mechanisms (Gao et al., 2015).

Based on field observations, laboratory experiments and numerical simulations, we created the initial conditions for the development of dunes in the two growth mechanisms by controlling sand availability:

- The dune experiment dedicated to the elongating mode started in November 2013. A dune field was flattened, covered with gravels and surrounded by a straw checkerboard to limit both sand availability and sand flux from outside (Fig. 1a of the main manuscript). The gravel area has a rectangular shape with one side parallel to the northwest-southeast direction, i.e., the direction of the prevailing wind. Perpendicularly to this direction, two isolated conical sand heaps sand were deposited in order to create the sources of sediment from which elongation can occur. These conical sand heaps are at least 5 meters from the straw checkerboard (maximum height of 20 cm) to minimize the surface roughness upstream of these areas of loose sediment. The sand heap to the northeast reached a height of 3 m, the one to the southwest a height of 2.5 m.

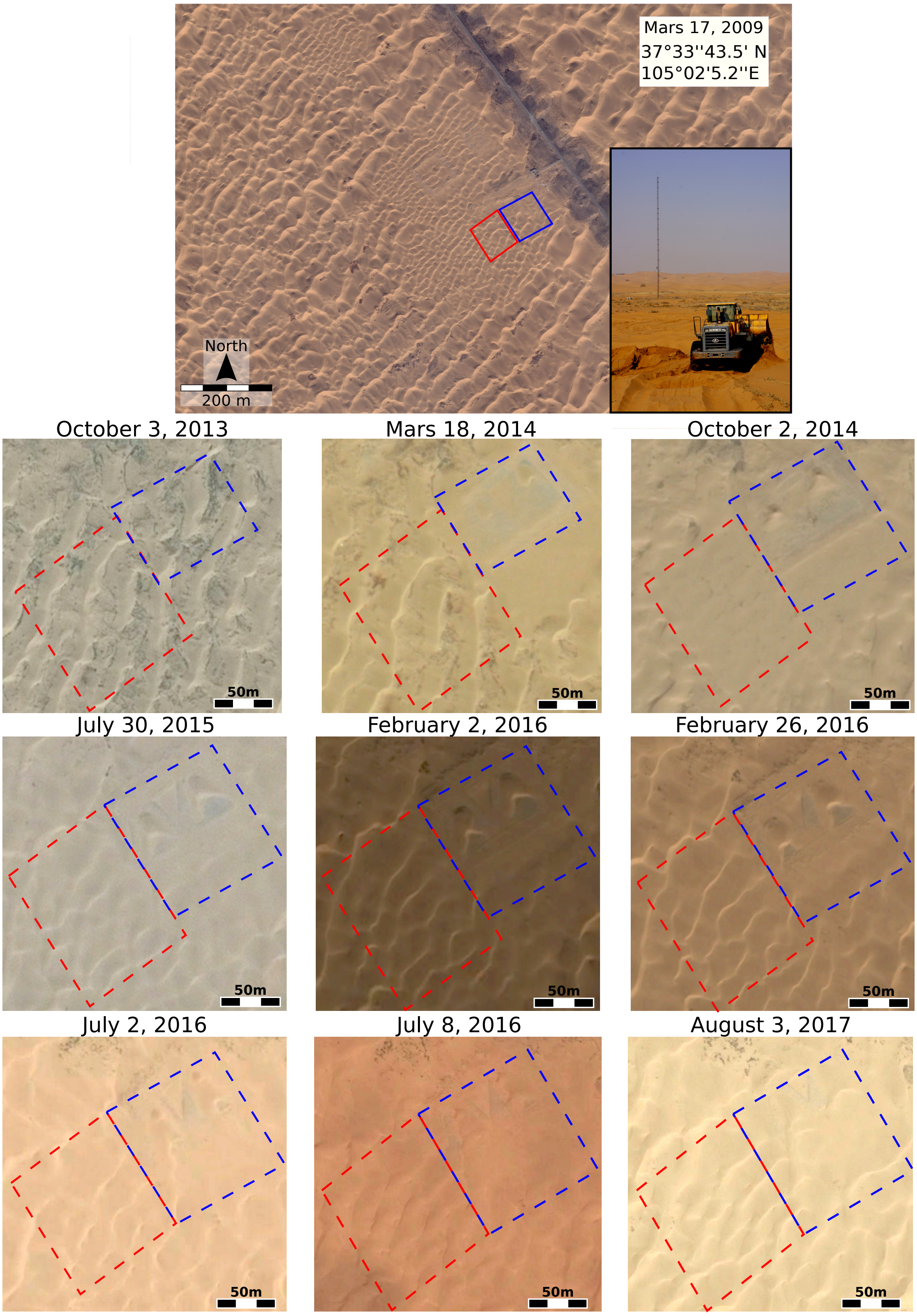

Figure S5: The landscape scale experiments on satellite images. The first flattening dates from December 2007. The development of dunes from April 30, 2008 to October 31, 2011 has been used by Ping et al. (2014) to validate theoretical predictions about dune orientations in multidirectional wind regimes. The new set of experiments analyzed in the present study focus on the two dune growth mechanisms. In November 2013, two sand heaps were deposited on a flat gravel bed to investigate the elongating mode Courrech du Pont et al. (2014). On the southwest border of this experiment, a sand bed have been flattened in April 2014. Regular topographic surveys document dune growth from November 2013 to November 2017 and can be compared to these satellite images (courtesy of Google Earth). Note the spontaneous development of the bed instability from October 2014 to July 2015 and the rapid elongation of the southern arm of the asymmetric barchan to the southwest in the spring 2016.

- The flat sand bed experiment dedicated to the dune instability started in April 2014. Pre-existing dunes were leveled to form a flat rectangular bed 100 m long and 75 m wide (Fig. 1c of the main manuscript). The long axis of this rectangular area is aligned with the direction of the primary wind (Lü et al., 2021).

All these rearrangements as well as the initial conditions and the subsequent evolution of the bedforms can be visualized using historical imagery from Google Earth (Fig. S5). We also monitored dune growth from November 2013 to November 2017 thanks to a series of topographic surveys using a ground-based laser scanner.

4.1 Dune elongation

As expected from the permanent loss of sediment of dome dunes, at the tip of the horns of barchan dune (Hersen, 2004; Elbelrhiti et al., 2008; Zhang et al., 2014) or along the entire body of elongating dunes (Rozier et al., 2019), the volume of the sand heaps is continuously decreasing. Early observations of bedform dynamics also revealed that they were too small with respect to the amount of sediment transported between two wind reversals, so that the dunes lose the memory of the previous transport event and systematically take the characteristic crescentic shape of barchan dune (Fig. 2a of the main manuscript). Furthermore, considering the limited amount of space of the gravel bed and sand transport at the upstream end of the sand heap, it is necessary to maintain a fixed sediment source in order to prevent dune migration and promote dune elongation. For all these purposes, it has been necessary to regularly add sand to the tops of the isolated sand heaps. These additions of sand were limited by the height of the bulldozer shovel ($\approx$ 4 m). Fig. S6 shows the surface elevation of the elongating dune experiment after the different additions of sand. It also shows that there is a systematic increase of the amount of sediment within the experimental plot, reflecting the accumulation of sand in the straw checkerboard and the permanent input flux from outside. All these fluxes contributes to the increase of the volume of the isolated dunes. The resultant sand flux is also oriented to the south (Tab. S1), so that the output flux of the dune to the northeast feeds the one to the southwest. As a consequence, this southwestern dune increases in size at the expense of the other and becomes larger. It is the only one to display elongation from October 2015, when the dune became large enough to integrate the variability of the local wind regime. As numerically investigated by Rozier et al. (2019) under a similar bidirectional wind regime, this is also because the longitudinal sediment flux was large enough to initiate deposition at the end of its southern arm. In November 2015, this elongation forced us to add gravel downstream of the elongating arm to ensure low sand availability at the dune tip.

Fig. S7 shows views of the elongating dune from the side and both ends. As predicted by Rozier et al. (2019), the height and the width of the dune decrease linearly according to the distance to the source. In addition, transient slip faces may form downwind of the prevailing winds. Fig. S8 shows the surface elevation in the flat sand bed and the elongating dune experiments at different times. Two different colorbars and the change in topography between the two experiments are used to distinguish dune shape and orientation in the bed instability and the elongating modes. This

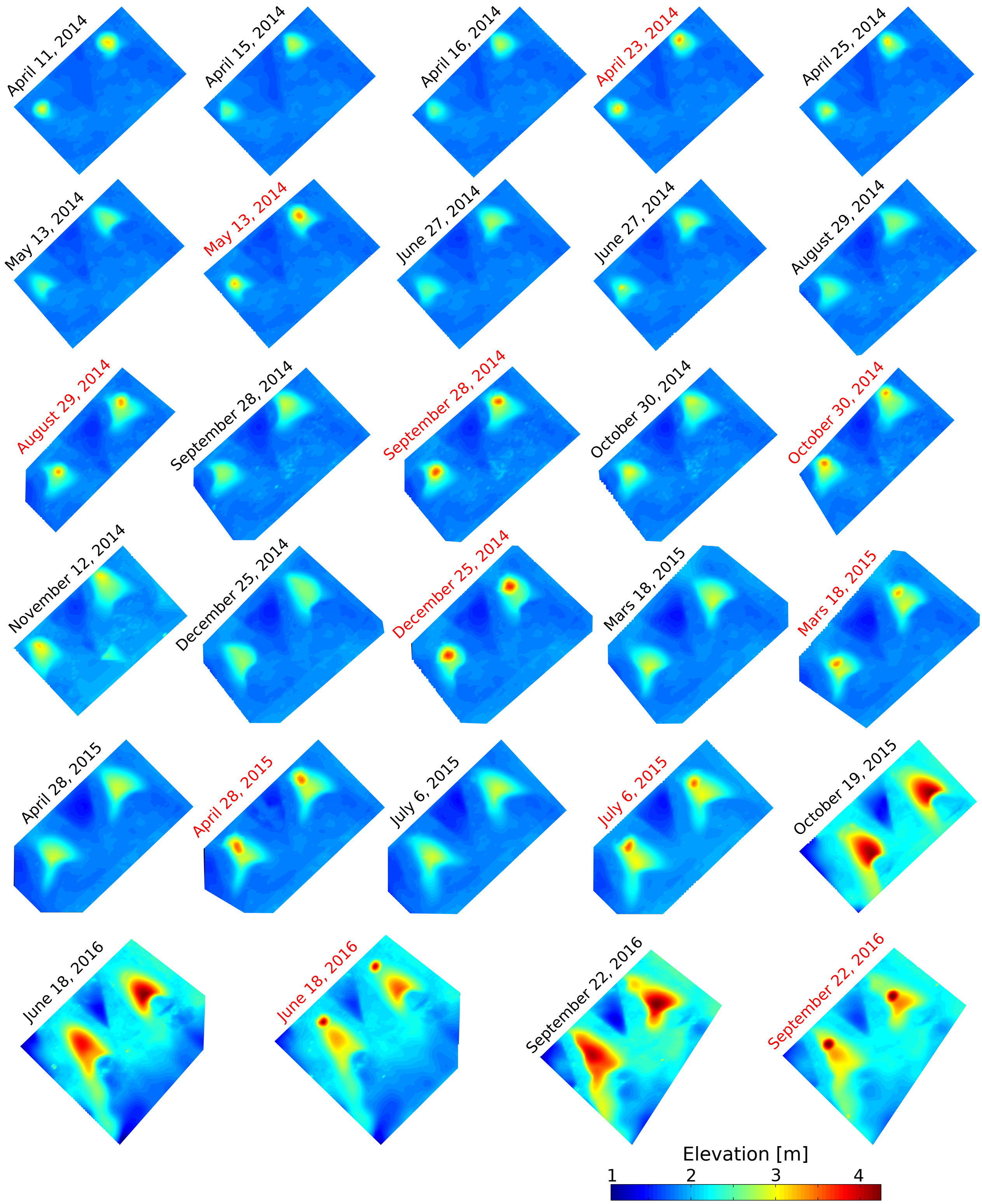

Figure S6: Evolution of bedforms and sand inputs in the elongating dune experiment. Surface elevation of the elongating dune experiment from April 2014 to September 2016. The dates of topographic surveys performed after an addition of sand are shown in red. Given these regular sand inputs, there is an increase in dune size over the duration of the elongating dune experiment. The southern arm of the asymmetric barchan dune to the southwest starts to elongate in the spring 2016. Note the continuous transition from dome to asymmetric barchan dunes and, in between, the reversal of barchan dunes.

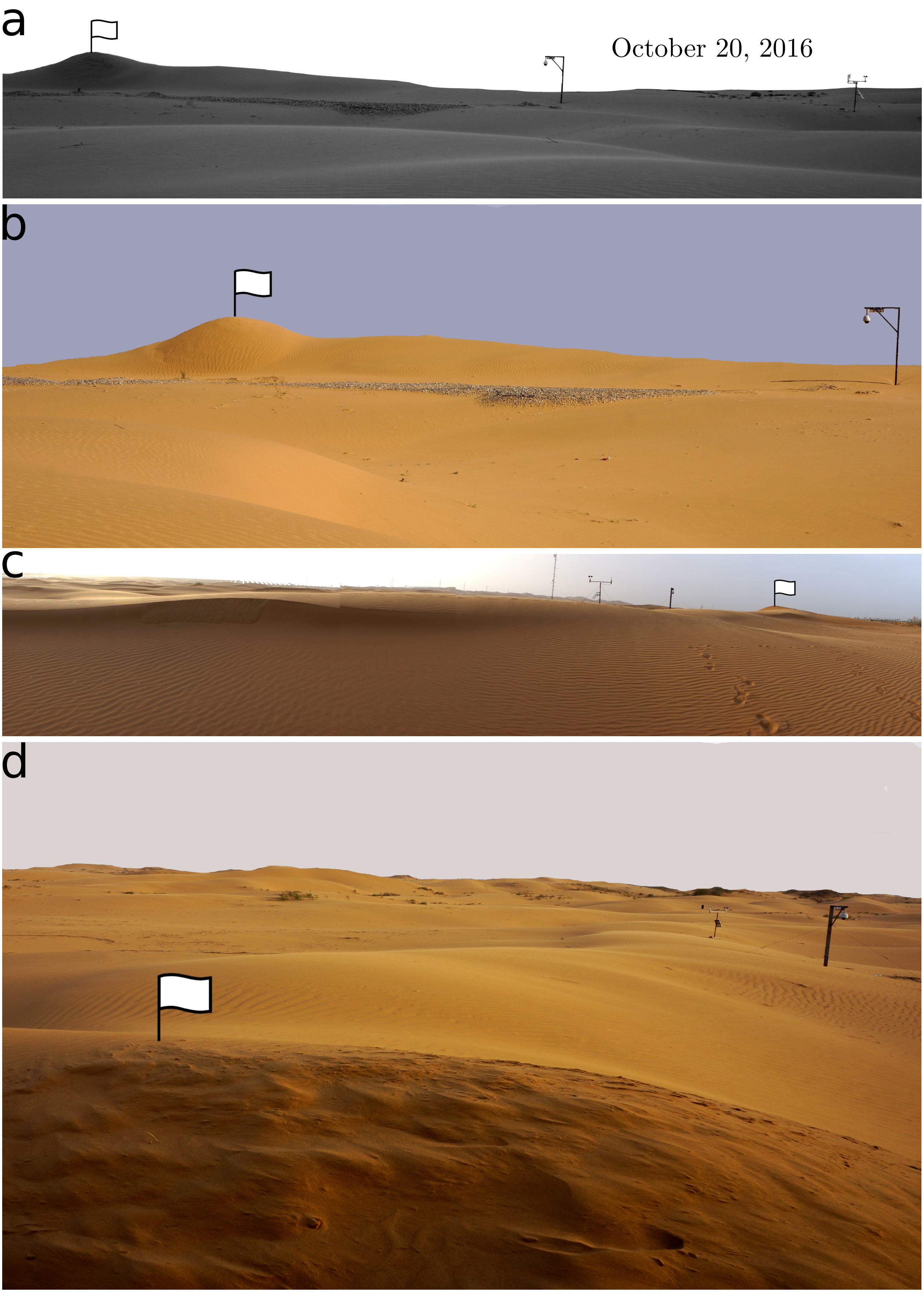

Figure S7: Elongating dunes on October 20, 2016. Pictures are taken the same day from the side (**a**,**b**), the tip (**c**) and the source area (**d**) of the elongating dune. The flag symbol shows the summit of the dune in all cases. The pole with a camera and the wind tower can be used as scale and reference points.

sequence of elevation maps reveal the migration of oblique dunes in the flat sand bed experiments and the elongation of the longitudinal dune on the gravel bed. The morphodynamics of these two types of dunes can then be studied over different time periods to estimate sand fluxes at their crests (Lü et al., 2017; Lucas et al., 2015).

A ground view in Fig. S8 also gives a panorama of the entire experimental dune field from a higher dune downstream. Two transect lines on this panorama are reported on the surface elevation derived from the laser scanner points at about the same time. One can see how difficult it is to differentiate between the two types of dunes in the field. Indeed, both of them have a low aspect ratio and their relative orientation $\Delta\alpha$ is often less than 25°. In addition, defects in zone of high sand availability tend to align with the elongating modes, while superimposed bedforms on the flanks of elongating dunes are likely to develop in the bed instability mode. This might explain why the coexistence of the two modes of dune orientation have not been systematically documented in the past during field investigations by geographers or geomorphologists.

4.2 Width, length and orientation of an isolated elongating dune

The methodology applied here to estimate the volume, width, length and orientation of the elongated dune can be performed in 2D or 3D on any type of isolated dune in order to provide a quantitative and reproducible characterization of its morphological properties.

An isolated dune is defined as a topographic anomaly $h(x, y)$ above a given threshold elevation. According to this elevation, the dune d is associated with an isoline $\mathcal{C}_\mathrm{d}$ surrounding a flat and horizontal closed surface $\mathcal{S}_d$. The volume of the dune is given by

$$\mathcal{V}_\mathrm{d} = \iint_{\mathcal{S}_\mathrm{d}} h(x, y)\, \mathrm{d}S \tag{17}$$

Using the topographic anomaly $h(x, y)$, we characterize the dune by the two first moments of the horizontal distribution of mass. The first moment gives the position of the center of mass. The second moment estimates the dispersion of mass in 2D. It is the covariance matrix or the so-called mass distribution matrix. The coordinates of the center of mass μ are given by

$$\mu_x = \frac{1}{\mathcal{V}_\mathrm{d}} \iint_{\mathcal{S}_d} x h(x, y)\, \mathrm{d}S \tag{18}$$

$$\mu_y = \frac{1}{\mathcal{V}_\mathrm{d}} \iint_{\mathcal{S}_d} y h(x, y)\, \mathrm{d}S \tag{19}$$

The second moment of the distribution of mass is a 2×2 matrix $\mathcal{M}$. Each element $\mathcal{M}_{ij}$ of this matrix is defined as

$$\mathcal{M}_{ij} = \widetilde{\mathcal{M}}_{ij} - \mu_i \mu_j. \tag{20}$$

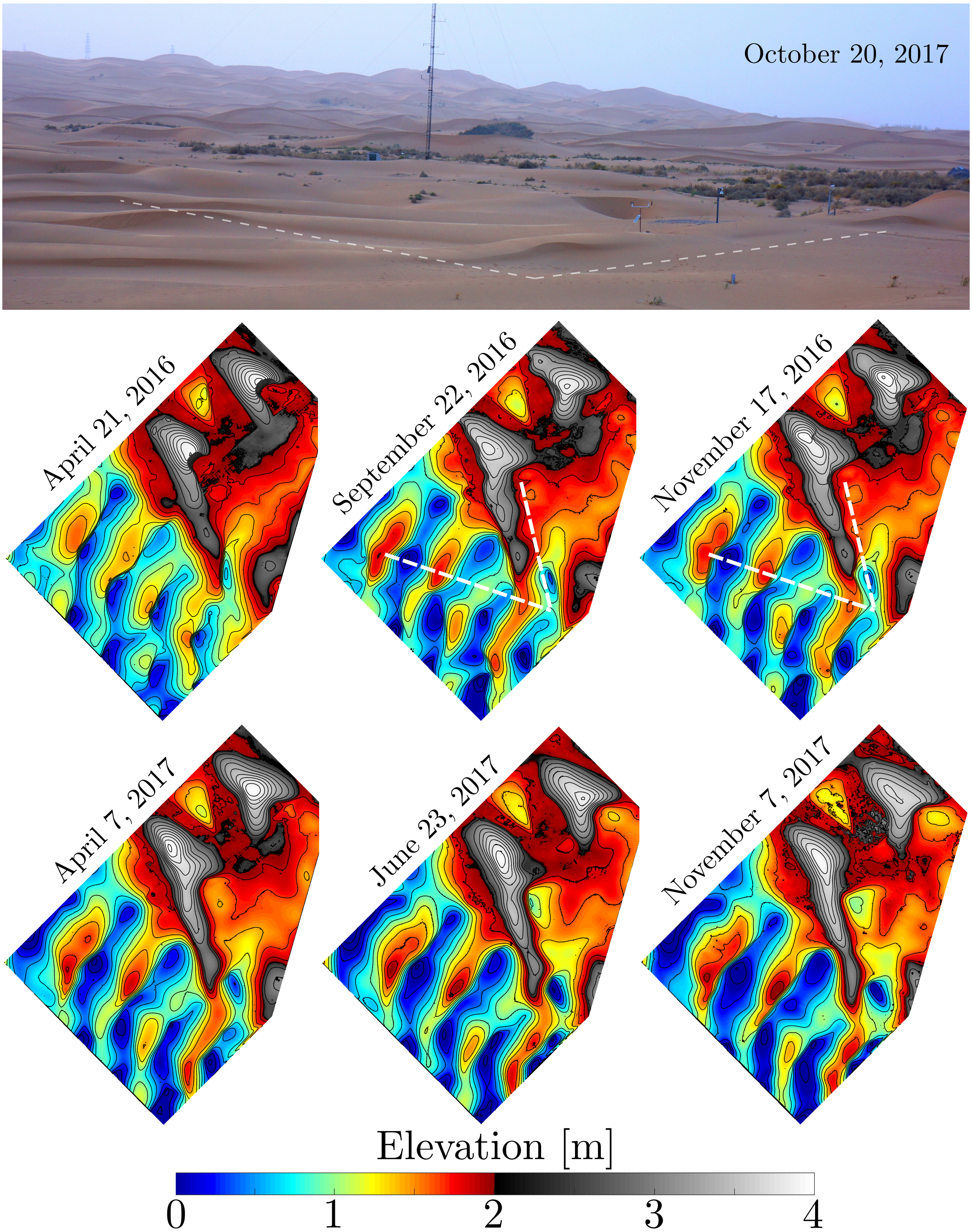

Figure S8: Surface elevation in the flat sand bed and the elongating dune experiments. Two distinct colorbars are used to distinguish the flat sand bed and the elongating dune experiments. The gravel bed elevation sets the transition and height with zero elevation. The top picture shows the experimental site on October 20, 2016 and two transect lines. They are reported on the surface elevation of September 22 and November 17, 2016. Note that, this example demonstrates that it is often difficult to distinguish between the two modes of dune orientation in the field or in ground view images. This is mainly due to the small dune aspect-ratio and the small angle $\Delta\alpha$ between the two modes of dune orientation (see Tab. S1).

where

$$\widetilde{\mathcal{M}}_{xx} = \frac{1}{\mathcal{V}_{\mathrm{d}}} \iint_{\mathcal{S}_d} x^2 h(x,y)\, \mathrm{d}S \tag{21}$$

$$\widetilde{\mathcal{M}}_{yy} = \frac{1}{\mathcal{V}_{\mathrm{d}}} \iint_{\mathcal{S}_d} y^2 h(x,y)\, \mathrm{d}S \tag{22}$$

$$\widetilde{\mathcal{M}}_{xy} = \frac{1}{\mathcal{V}_{\mathrm{d}}} \iint_{\mathcal{S}_d} xy h(x,y)\, \mathrm{d}S \tag{23}$$

We calculate the eigenvectors $\mathbf{V}_{1,2}$ and the corresponding eigenvalues $\lambda_1 \geq \lambda_2$ of the square matrix $\mathcal{M}$ to determine the principal orientations of the topographic anomaly (i.e., of the dune). These eigenstates may characterize quantitatively major morphological dune types. Nevertheless, it depends on the threshold elevation, which should be chosen according to the current environment. For isolated elongating dune, it is the height of the nonerodible bed on which they form.

The following properties are of special interest and are used to determine the orientation, the length and the width of the isolated elongating dunes:

- The primary orientation $\mathbf{V}_1$ gives the dune alignment.
- The largest eigenvalue λ_1 gives the standard deviation of the mass distribution along the primary orientation, i.e., the direction along which the dune is elongating. By analogy with the normal distribution, the length of the dune is taken equal to $4\lambda_1$. This estimation is validated by direct measurements of the length on the elevation maps.
- The secondary orientation $\mathbf{V}_2$ is perpendicular to the dune alignment and corresponds to the second eigenvalue λ_2. The dune width is taken equal to $4\lambda_2$. This estimation is validated by direct measurements of the width on the elevation maps.
- The λ_1/λ_2 ratio gives the horizontal dune aspect-ratio. It is by definition the length/width ratio shown in Fig. 4E of the main manuscript.

References

Courrech du Pont, S., Narteau, C., & Gao, X. (2014). Two modes for dune orientation. *Geology*, *42*(9), 743–746. doi: 10.1130/G35657.1

Dempster, A. P., Laird, N. M., & Rubin, D. B. (1977). Maximum likelihood from incomplete data via the em algorithm. *Journal of the Royal Statistical Society: Series B (Methodological)*, *39*(1), 1–22.

Durán, O., Claudin, P., & Andreotti, B. (2011). On aeolian transport: Grain-scale interactions, dynamical mechanisms and scaling laws. *Aeolian Research*, *3*(3), 243–270.

Elbelrhiti, H., Andreotti, B., & Claudin, P. (2008). Barchan dune corridors: field characterization and investigation of control parameters. *J. Geophys. Res.*, *113*(F02S15).

Field, J., & Pelletier, J. (2018). Controls on the aerodynamic roughness length and the grain-size dependence of aeolian sediment transport. *Earth Surface Processes and Landforms*, *43*, 2616–2626.

Fryberger, S. G., & Dean, G. (1979). Dune forms and wind regime. *A study of global sand seas*, *1052*, 137–169.

Gadal, C., Narteau, C., du Pont, S. C., Rozier, O., & Claudin, P. (2019). Incipient bedforms in a bidirectional wind regime. *Journal of Fluid Mechanics*, *862*, 490–516.

Gao, X., Narteau, C., Rozier, O., & Courrech du Pont, S. (2015). Phase diagrams of dune shape and orientation depending on sand availability. *Scientific reports*, *5*, 14677. doi: 10.1038/srep14677

Hersen, P. (2004, February). On the crescentic shape of barchan dunes. *European Physical Journal B*, *37*(4), 507-514.

Hunter, R. E., Richmond, B. M., et al. (1983). Storm-controlled oblique dunes of the oregon coast. *Geological Society of America Bulletin*, *94*(12), 1450–1465.

Iversen, J. D., & Rasmussen, K. R. (1999). The effect of wind speed and bed slope on sand transport. *Sedimentology*, *46*(4), 723–731.

Jackson, P. S., & Hunt, J. C. R. (1975). Turbulent wind flow over a low hill. *Q. J. R. Meteorol. Soc.*, *101*, 929.

Lü, P., Narteau, C., Dong, Z., Claudin, P., Rodriguez, S., An, Z., … Courrech du Pont, S. (2021). Direct validation of dune instability theory. *Proceedings of the National Academy of Sciences*, *118*(17). doi: 10.1073/pnas.2024105118

Lü, P., Narteau, C., Dong, Z., Rozier, O., & Courrech Du Pont, S. (2017). Unravelling raked linear dunes to explain the coexistence of bedforms in complex dunefields. *Nature Communications*, *8*, 14239.

Lucas, A., Narteau, C., Rodriguez, S., Rozier, O., Callot, Y., Garcia, A., & Courrech du Pont, S. (2015). Sediment flux from the morphodynamics of elongating linear dunes. *Geology*, *43*(11), 1027–1030.

Owen, P. R. (1964). Saltation of uniformed sand grains in air. *J. Fluid. Mech.*, *20*, 225–242.

Pearce, K. I., & Walker, I. J. (2005). Frequency and magnitude biases in the 'Fryberger' model, with implications for characterizing geomorphically effective winds. *Geomorphology*, *68*(1), 39–55.

Ping, L., Narteau, C., Dong, Z., Zhang, Z., & Courrech du Pont, S. (2014). Emergence of oblique dunes in a landscape-scale experiment. *Nature Geoscience*, *7*, 99–103. doi: 10.1038/ngeo2047

Rozier, O., Narteau, C., Gadal, C., Claudin, P., & Courrech du Pont, S. (2019). Elongation and stability of a linear dune. *Geophysical Research Letters*, *46*, 14521–14530. doi: 10.1029/2019GL085147

Rubin, D., & Hunter, R. (1987). Bedform alignment in directionally varying flows. *Science*, *237*, 276–278.

Sherman, D. J., & Farrell, E. J. (2008). Aerodynamic roughness lengths over movable beds: Comparison of wind tunnel and field data. *Journal of Geophysical Research: Earth Surface*, *113*(F02S08).

Tsoar, H. (2005). Sand dunes mobility and stability in relation to climate. *Physica A*, *357*(1), 50–56.

Ungar, J., & Haff, P. (1987). Steady state saltation in air. *Sedimentology*, *34*(2), 289–299.

Zhang, D., Yang, X., Rozier, O., & Narteau, C. (2014). Mean sediment residence time in barchan dunes. *J. Geophys. Res.*, *119*, 451–463. doi: 10.1002/2013JF002833